Geophysical Research Letters

RESEARCH LETTER
10.1029/2026GL123397

# Cloud-Rain Vertical Inconsistency Increases IMERG Precipitation Uncertainty

**Haoqian Zhang**[1], **Aoqi Zhang**[1,2], **and Yilun Chen**[1,2]

[1]School of Atmospheric Sciences, Sun Yat-sen University, Zhuhai, China, [2]Southern Marine Science and Engineering Guangdong Laboratory (Zhuhai), Zhuhai, China

**Abstract** IMERG accuracy is limited by the vertical inconsistency between satellite-observed cloud-top information and the true vertical structure of precipitation. Using FY-3G Precipitation Measurement Radar (PMR) observations as reference and FY-4B cloud-top parameters, we investigate the vertical-structure sources of IMERG retrieval errors during the 2024 pre-summer rainy season in South China. IMERG intensity biases vary markedly with classification framework: when classified by cloud-top height (CTH), IMERG overestimates precipitation associated with high clouds, whereas classification by storm-top height (STH) reveals significant underestimation. IMERG detection accuracy increases rapidly as STH exceeds 7.5 km and remains above 0.8. Three cloud-rain vertical inconsistency regimes are identified: severe missed warm-cloud precipitation (STH $\approx$ CTH $<$ 5 km), overestimated precipitation area in anvil clouds (CTH $\gg$ STH), and underestimated precipitation intensity in convective cores (STH $\approx$ CTH $>$ 12 km). These results suggest cloud-rain height difference as a useful correction factor for future multisource precipitation retrieval algorithms.

**Plain Language Summary** Satellite rainfall products often contain systematic errors because satellites mainly observe cloud tops, not the full vertical structure of precipitation. This problem is especially important during the pre-summer rainy season in South China, where warm rain, anvil clouds, and deep convection frequently coexist. Using FY-3G precipitation radar and FY-4B cloud-top observations, we show that IMERG errors are closely related to cloud-rain vertical inconsistency. IMERG tends to miss warm rain, overestimate rainfall area in anvil clouds, and underestimate rainfall intensity in deep convective cores. We also find that IMERG detects precipitation much more reliably once storm-top height exceeds about 7.5 km. These results suggest that cloud-rain height difference could provide a useful physical constraint for improving future satellite precipitation retrieval algorithms.

**Key Points:**

- IMERG errors over South China are strongly controlled by cloud-rain vertical inconsistency
- IMERG detection skill increases rapidly once storm-top height exceeds about 7.5 km
- Missed warm rain, anvil overestimation, and convective-core underestimation explain the main IMERG errors

**Supporting Information:**

Supporting Information may be found in the online version of this article.

**Correspondence to:**

Y. Chen,
chenylun3@mail.sysu.edu.cn

**Citation:**

Zhang, H., Zhang, A., & Chen, Y. (2026). Cloud-rain vertical inconsistency increases IMERG precipitation uncertainty. *Geophysical Research Letters*, *53*, e2026GL123397. https://doi.org/10.1029/2026GL123397

Received 1 APR 2026
Accepted 7 MAY 2026

**Author Contributions:**

**Conceptualization:** Haoqian Zhang, Aoqi Zhang, Yilun Chen
**Data curation:** Haoqian Zhang
**Funding acquisition:** Yilun Chen
**Methodology:** Haoqian Zhang, Aoqi Zhang, Yilun Chen
**Project administration:** Yilun Chen
**Validation:** Haoqian Zhang
**Visualization:** Haoqian Zhang
**Writing – original draft:** Haoqian Zhang
**Writing – review & editing:** Haoqian Zhang, Aoqi Zhang, Yilun Chen



## 1. Introduction

Integrated Multi-satellitE Retrievals for GPM (IMERG) is a core precipitation product developed under the Global Precipitation Measurement (GPM) mission. It is calibrated against the GPM Combined Radar–Radiometer product (CORRA), which combines observations from the Dual-frequency Precipitation Radar (DPR) and the GPM Microwave Imager (GMI), while also integrating scattering signals from passive microwave(PMW) sensors and cloud-top information from geostationary infrared(IR) sensors, making it a key data set for global precipitation monitoring (Hou et al., 2014; Huffman et al., 2020; Skofronick-Jackson et al., 2017). Previous studies have shown that IMERG captures precipitation diurnal variability and occurrence frequency reasonably well (Dezfuli et al., 2017; Montoya Duque et al., 2023). However, IMERG retrieval performance remains limited over complex regional precipitation systems, especially during the pre-summer rainy season in South China, where frequent cold–warm air interactions and the coexistence of convective and stratiform precipitation create a particularly challenging environment for accurate retrieval (S. Chen et al., 2025; Y. Zhang et al., 2023).

Precipitation systems during the pre-summer rainy season in South China are highly complex and often exhibit a double-rainband structure, with frontal and warm-sector precipitation occurring simultaneously (Chen et al., 2018; Han et al., 2021; Li & Du, 2021). The northern frontal rainband is typically associated with low-level horizontal shear and surface frontal systems, whereas the southern warm-sector rainband develops under weak large-scale forcing but favorable mesoscale conditions (Z.-h. Guo et al., 2024). These two rainbands also differ substantially in microphysical structure: compared with frontal precipitation, warm-sector convection is generally characterized by stronger convective intensity, larger raindrops, and higher liquid water content (Han et al., 2021).

Spaceborne precipitation radar observations further show that these microphysical properties vary systematically with frontal distance, with small but numerous raindrops near the front (0–100 km), where ice-phase processes dominate, and larger raindrops farther from the front (200–300 km), where ice- and liquid-phase processes coexist (Zuo et al., 2025). Such coexisting and spatially evolving rainbands generate pronounced heterogeneity in the three-dimensional structure of precipitation, making satellite precipitation retrieval particularly challenging in this region.

A key source of this uncertainty is the limited ability of satellite-observed cloud properties to fully represent the vertical structure of precipitation. Infrared sensors measure only cloud-top brightness temperature, while over land, passive microwave retrievals primarily depend on high-frequency scattering signatures from ice-phase particles to infer precipitation indirectly. Over ocean, in contrast, passive microwave retrievals can also use low-frequency emission signals from near-surface hydrometeors (Ferraro, 1997; Stephens et al., 2007). As a result, satellite-observed cloud-top characteristics are often decoupled from surface rainfall within the vertical column. Extremely low cloud-top brightness temperatures, for example, may correspond either to intense precipitation cores in deep convection or to nonprecipitating cirrus anvils. Conversely, warm-cloud systems can produce substantial rainfall, but these warm-sector heavy precipitation events, which are typical during the pre-summer rainy season in South China, are often missed (Wang et al., 2018). In fact, pioneering process-based evaluations have identified this inherent misinterpretation of warm clouds and low-ice-path anvils as a fundamental source of IMERG retrieval errors (Maranan et al., 2020). Therefore, rather than a simple vertical offset, the highly variable relationship between cloud-top properties and surface precipitation for IR retrievals, combined with the inherent absence of frozen hydrometeors required for PMW scattering signals in warm clouds, constitute the primary sources of error in IMERG.

Quantifying retrieval errors associated with cloud-rain vertical mismatch requires fine-scale three-dimensional validation. Yet conventional evaluations of satellite precipitation products rely primarily on rain gauges and ground-based radar networks (Wang et al., 2021). These approaches can effectively characterize biases in precipitation amount and horizontal distribution, but they provide limited insight into the vertical physical origins of retrieval errors (Turk et al., 2021). Previous studies have shown that IMERG errors vary markedly with season and precipitation intensity, with overestimation common for moderate-to-heavy rainfall in the warm season and underestimation typical for light precipitation in the cold season (Derin et al., 2021). During extreme precipitation events, false alarms and missed detections may dominate the total error budget (H. Guo et al., 2024; Pradhan et al., 2023). However, without direct observations of precipitation vertical structure, it remains difficult to determine whether these errors are caused by algorithm saturation, anvil contamination, detection-threshold limitations, or the physical absence of ice-phase scattering signatures (Grecu et al., 2016; Shang et al., 2025; Smalley et al., 2014).

The Fengyun-3G (FY-3G) satellite, China's first precipitation mission launched in April 2023, provides a new opportunity to overcome these observational limitations. Its dual-frequency Precipitation Measurement Radar (PMR) has active three-dimensional profiling capability comparable to that of the GPM Dual-frequency Precipitation Radar (DPR), enabling direct observation of precipitation vertical structure and accurate identification of storm-top height (STH), the true upper boundary of precipitating systems (P. Zhang et al., 2023). Recent studies have shown strong consistency between PMR observations and China's ground-based weather radar network (He et al., 2025; Shang et al., 2025). Combining FY-3G-derived STH with cloud-top height (CTH) from the Fengyun-4B (FY-4B) geostationary satellite establishes a unified vertical coordinate framework for examining cloud-rain structure. Because FY-3G PMR is independent of the GPM DPR/GMI retrieval framework used to constrain IMERG, it provides a more independent reference for evaluation and helps avoid the overlapping use of reference data. In contrast, validation based directly on DPR would primarily assess the best-constrained portion of IMERG, closely linked to GMI retrievals, and would therefore be less representative of overall IMERG performance. This active-passive three-dimensional framework therefore enables a more objective assessment of IMERG retrieval errors while reducing interference from misleading cloud-top signals.

Here we use FY-3G PMR observations during the pre-summer rainy season in South China to quantify how IMERG retrieval errors respond to cloud-rain height difference, thereby clarifying the role of vertical cloud-rain structure in retrieval uncertainty and providing physical guidance for improving active-passive collaborative precipitation retrievals.

## 2. Data and Methods

This study uses active radar observations, multisource merged precipitation products, and high-temporal-resolution geostationary satellite data. Our analysis focuses on the 2024 pre-summer rainy season (April–June) in South China, a period characterized by frequent cold-warm air interactions and the frequent coexistence of convective and stratiform precipitation (Luo et al., 2017).

We use the Integrated Multi-satellitE Retrievals for GPM, a multisource precipitation product developed within the GPM framework (Hou et al., 2014). IMERG provides precipitation estimates at 0.1° spatial and half-hourly temporal resolution. According to processing latency and calibration level, IMERG is released as Early Run (IMERG-E), Late Run (IMERG-L), and Final Run (IMERG-F) products (Huffman et al., 2020). IMERG-E and IMERG-L are near-real-time products available about 4 and 12 hr after observation, respectively, whereas IMERG-F is a post-processed product that includes gauge-based bias correction and generally achieves higher accuracy. Previous studies have shown that IMERG substantially outperforms the earlier TMPA 3B42-V7 product and ranks among the best-performing global satellite precipitation data sets (Tang et al., 2016, 2020). In this study, we evaluate the latest GPM IMERG V07 Final half-hourly precipitation product.

We further use near-surface precipitation rate from the FY-3G PMR Level-2 product as the reference for evaluating IMERG precipitation estimates. The dual-frequency Precipitation Measurement Radar (PMR) onboard FY-3G can penetrate cloud layers to retrieve the vertical structure of precipitation and identify storm-top height (STH), defined here as the highest altitude reached by detectable precipitation particles. Like the GPM DPR, FY-3G PMR provides active three-dimensional observations of precipitating systems. Previous comparisons with China's ground-based weather radar network demonstrated reliable data quality, with a correlation coefficient of 0.87 and a bias of only 0.89 dB (He et al., 2025; Shang et al., 2025). Recent evaluations further show strong consistency between FY-3G PMR and GPM DPR in both light-precipitation detection threshold and storm-top-height retrieval capability (Liu et al., 2025), supporting the use of FY-3G PMR as an independent reference for IMERG evaluation.

To characterize cloud-top properties, we also use Level-2 cloud-top height (CTH) and cloud-top temperature (CTT) products from the Advanced Geosynchronous Radiation Imager (AGRI) onboard FY-4B. CTH represents the maximum height of the visible cloud top and provides a measure of the upper boundary of cloud development (Huo et al., 2020; Liu et al., 2020; Yang et al., 2021). CTT denotes the temperature at the cloud top. The high temporal resolution of AGRI (≤15 min) enables precise collocation with low-Earth-orbit satellite observations.

To reduce systematic biases caused by differences in sensor geometry and resolution, we constructed a pixel-level spatiotemporal collocation framework. PMR overpass time was used as the temporal reference, and the mean observation time of valid pixels within each scan swath was used to align the corresponding IMERG 30-min window, such that the time difference between PMR and IMERG was constrained to within 15 min. For FY-4B, the observation nearest in time to the PMR overpass was selected for cloud classification. All data sets were mapped to a common $0.1° \times 0.1°$ grid, consistent with the native resolution of IMERG. PMR swath data and FY-4B observations were resampled to this grid using KD-tree nearest-neighbor interpolation, with each target grid cell assigned the value of the nearest valid PMR pixel (Orenstein, 1982). To prevent spatial smearing across swath edges during resampling (Kidd et al., 2003), the search radius was limited to 0.1°, and grid cells beyond this threshold were treated as invalid. A polygonal swath boundary was then defined from the outermost PMR latitude-longitude coordinates, and only IMERG and PMR pixels within this boundary were retained. This ensured that all subsequent pixel-level comparisons were confined to the radar-observed domain. Finally, a precipitation threshold of 0.1 mm $hr^{-1}$ was applied to exclude trace precipitation and nonprecipitating cloud plumes when evaluating passive-retrieval performance under different physical conditions (Petersen et al., 2020; Wang et al., 2021). The detailed mathematical definitions and formulations of the categorical metrics (POD, FAR, and HSS) and continuous metrics (ME, MAE) used in this study are provided in Text S1 of Supporting Information S1.

In addition to conventional metrics such as correlation coefficient (CC) and root mean square error (RMSE), we use the object-based Structure-Amplitude-Location (SAL) method to characterize precipitation-product performance in terms of spatial structure, intensity, and displacement(Wernli et al., 2008). Precipitation objects were identified by applying a threshold of 0.1 mm $hr^{-1}$ to both PMR and IMERG precipitation fields, and contiguous grid cells exceeding this threshold were treated as individual precipitation objects for the SAL calculation. SAL

quantifies these attributes with three components: structure (S), amplitude (A), and location (L). We then interpret all error metrics in a vertical coordinate framework defined by storm-top height (STH) and cloud-top height (CTH). The cloud-rain height difference is defined as $\Delta H = \mathrm{CTH} - \mathrm{STH}$. Cases with $\Delta H \approx 0$ are regarded as vertically consistent, as in mature deep convective cores, whereas cases with $\Delta H \gg 0$ indicate strong cloud-rain vertical mismatch, such as thick upper-level anvil clouds accompanied by weak or no lower-level precipitation (Liu et al., 2007). This framework allows us to examine how satellite precipitation retrieval errors vary with cloud-rain height difference and to infer the underlying physical mechanisms.

## 3. Results

Figure 1 shows a representative heavy-precipitation case during the 2024 pre-summer rainy season in South China, illustrating differences between IMERG and FY-3G PMR in depicting precipitation spatial structure. Figure 1a compares the infrared brightness-temperature field with precipitation boundaries from the two satellite products. IMERG captures the overall orientation and morphology of the main rainband reasonably well, but its retrieved precipitation area (red dashed line) is markedly larger than the actual precipitation area detected by FY-3G PMR (blue solid line) (Rajagopal et al., 2021). This areal overestimation is particularly evident along the edges of cold clouds, especially in convective anvil regions with very low brightness temperatures (Cui et al., 2020).

To quantify this difference in spatial distribution, we calculated the three SAL components from the precipitation objects identified in Figures 1b and 1c (PMR) and (IMERG). The resulting SAL metrics indicate clear structural bias in IMERG. A positive structure term ($S = 1.60$) indicates pronounced spatial overextension, while a negative amplitude term ($A = -0.15$) indicates underestimation of overall precipitation intensity. The location term ($L = 0.09$) suggests that this peripheral overextension also shifts the identified precipitation centroid. These results confirm that the precipitation area retrieved by IMERG is overly broad because it includes convective anvil regions containing suspended ice particles that do not produce effective surface rainfall (Cui et al., 2020).

To quantify how IMERG errors depend on vertical structure, Table 1 and Figure 2 summarize IMERG detection performance when stratified by cloud-top temperature, cloud-top height, and storm-top height.

Table 1 reveals a clear systematic bias. In low-cloud or warm-rain precipitation regimes, IMERG generally shows low probability of detection (POD) but high false alarm rate (FAR), and extremely low Heidke Skill Score (HSS), indicating limited ability to identify true precipitation events and a tendency toward spurious detections in these environments. However, when precipitation is classified by storm-top height, IMERG detection performance in low-cloud cases improves, suggesting that STH-based classification better captures the vertical conditions relevant to precipitation detection.

Figure 2 further shows a nonlinear increase in IMERG probability of detection with increasing vertical development of precipitation. In warm-rain or shallow precipitation conditions (e.g., CTH < 4 km or CTT > 273 K), POD is generally below 0.4, whereas FAR exceeds 0.8 and HSS approaches zero (indicating almost no predictive skill relative to random chance). As precipitation vertical extent increases, POD rises rapidly. When stratified by storm-top height (Figure 2c), POD remains slightly above 0.4 even for shallow precipitation (STH < 4 km). Once STH exceeds approximately 7.5 km (the typical freezing level during the pre-summer rainy season in South China is around 5 km), POD increases sharply and stabilizes above 0.8. This threshold-like transition indicates that ice-phase scattering begins to provide a stronger constraint for passive microwave retrieval, substantially enhancing the detection of deep convective precipitation (Gong & Wu, 2017).

These results indicate that IMERG detection performance is strongly controlled by the vertical structure of precipitating clouds, with the effective involvement of ice-phase processes playing a critical role in the detection of deep convective precipitation. This sensitivity to cloud vertical development is expressed not only in detection skill, but also in the quantitative estimation of precipitation intensity.

Precipitation-intensity evaluation further reveals a pronounced asymmetric error pattern in IMERG (Figure 3). When cases are classified by cloud-top parameters (Figures 3a and 3b), IMERG shows a clear positive bias in rain-rate estimation. As cloud vertical development reaches deep-convective levels (e.g., CTH > 10 km), the mean rain rate retrieved by IMERG increasingly exceeds the PMR reference. In parallel, the mean error (ME) shifts to positive values, indicating a systematic overestimation, while the mean absolute error (MAE) also increases significantly, reflecting large absolute deviations.

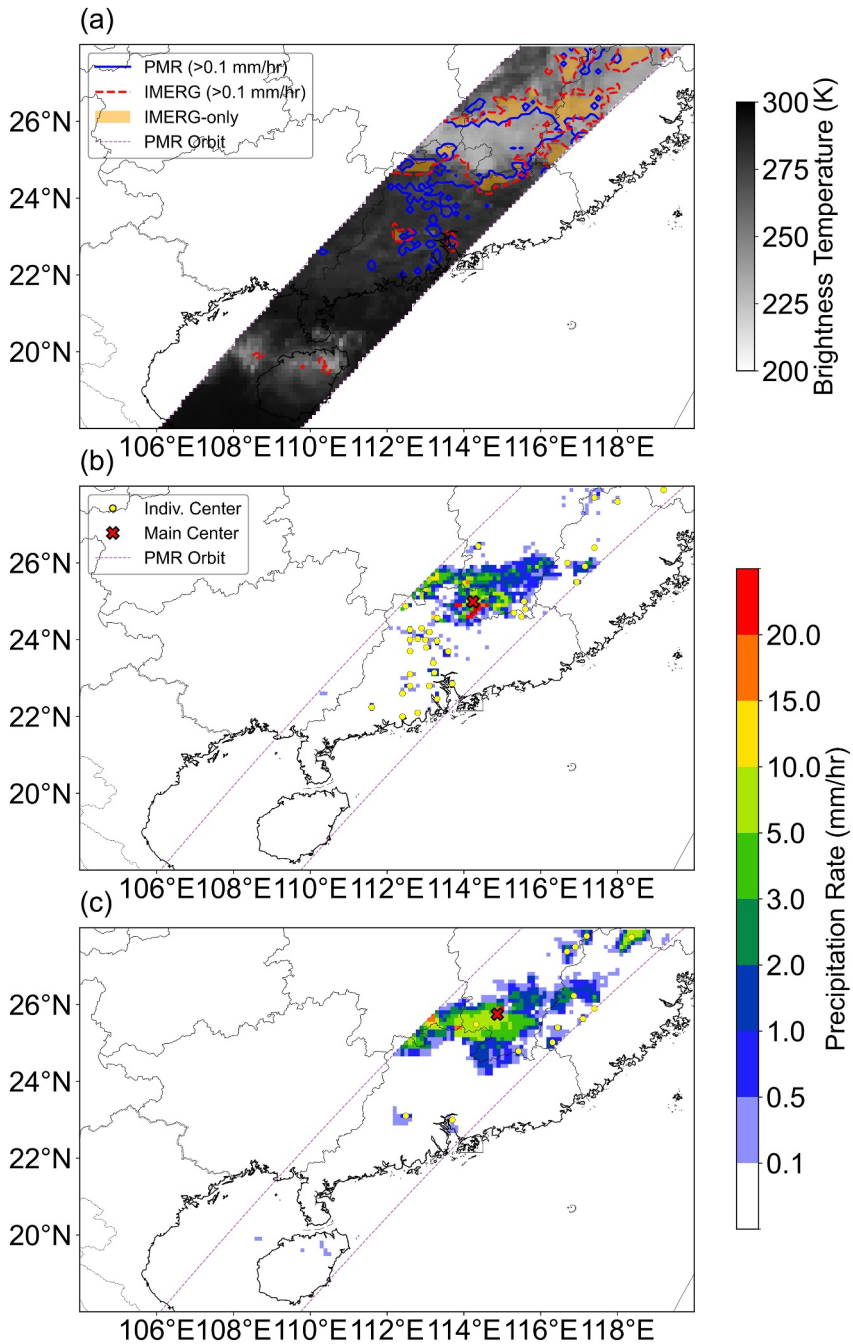


**Figure 1.** Precipitation extent of PMR and IMERG during a precipitation event in 2024 (a). Spatial distribution of the main precipitation objects identified by the SAL method for PMR (b) and IMERG (c).

However, when precipitation intensity is examined in the storm-top framework (STH; Figure 3c), the bias reverses. For the same deep convective systems (STH > 10 km), the PMR reference mean rain rate becomes larger than that retrieved by IMERG. Consistently, the mean error (ME) shifts rapidly to negative values (approaching −10 mm/hr for extreme STH), while the MAE spikes simultaneously, highlighting severe underestimation of extreme rainfall. This sharp contrast—systematic overestimation in the cloud-top framework versus pronounced underestimation in the storm-top framework—highlights a broader limitation of IR-based precipitation retrieval approaches used when PMW constraints are unavailable: cloud-top properties alone cannot adequately represent

**Table 1**
*Evaluation of IMERG Precipitation Detection Performance Based on Different Classification Criteria*

| Classification basis | Category | POD | HSS | FAR |
|---|---|---|---|---|
| Cloud-Top Temp | Warm Rain(>273 K) | 0.275 | 0.938 | 0.912 |
| | Moderate height clouds(235–273 K) | 0.633 | 0.776 | 0.696 |
| | Deep Convection(<235 K) | 0.901 | 0.352 | 0.476 |
| Cloud-Top Height | Shallow precipitation (<4 km) | 0.305 | 0.933 | 0.891 |
| | Moderate height clouds(4–10 km) | 0.575 | 0.816 | 0.725 |
| | Deep Convection(>10 km) | 0.881 | 0.354 | 0.498 |
| Storm-Top Height | Shallow precipitation (<4 km) | 0.480 | 0.115 | 0.725 |
| | Moderate height storms(4–8 km) | 0.758 | 0.265 | 0.427 |
| | Deep Convection(>8 km) | 0.926 | 0.263 | 0.306 |

the true three-dimensional vertical structure of precipitation intensity. As a result, opposite bias signatures emerge under different vertical reference frameworks.

## 4. Discussion

Taken together, the above results identify three typical retrieval-error regimes in IMERG: (a) severe missed detection of warm-cloud precipitation (STH ≈ CTH < 5 km); (b) overestimation of precipitation area in anvil regions (CTH ≫ STH); and (c) underestimation of precipitation intensity in convective cores (STH ≈ CTH > 12 km). The physical origins of these three error regimes are discussed below and illustrated schematically in Figure 4.

In the warm-rain regime on the left side of Figure 4, where cloud tops remain below the 0°C level during the pre-summer rainy season in South China (about 5 km), hydrometeors are almost entirely liquid and ice-phase particles are effectively absent. Under these conditions, IMERG faces an inherent difficulty because land PMW retrievals rely strongly on high-frequency scattering signatures from frozen hydrometeors to infer surface precipitation. When such ice-scattering signatures are weak or absent, substantial surface rainfall may be missed, and retrievals are more easily affected by surface background emission and other environmental influences (Sekaranom et al., 2019). This explains the two main features observed in the low-CTH regime of Figure 2: very low probability of detection and persistently high false alarm rate under strong background surface-radiation interference.

The positive bias seen in Figure 3 under cloud-top-height classification mainly originates from the anvil regime shown in Figure 4. During the mature stage of intense convective systems, strong upper-level winds spread ice crystals lofted from the convective core outward, producing extensive cirrus anvils with very high cloud tops and extremely low cloud-top temperatures (CTH > 14 km). Zhang et al. (2022), using GPM DPR and FY-4A observations, documented a similar two-layer advective cloud structure: the very cold upper cloud shield is often transported from vigorous convection but produces little or no surface rainfall, whereas actual precipitation may be confined to the underlying warm cloud layer. When such regions lie outside the active-radar swath, infrared sensors can misidentify them as deep convective cores because of their extremely cold cloud tops (Cui et al., 2020). Meanwhile, passive microwave retrievals are also contaminated by nonprecipitating scattering from suspended ice crystals within the anvil. Furthermore, due to the time required for precipitation particles to descend from high storm tops, a spatiotemporal offset exists between the satellite-captured instantaneous cloud-top signals and the actual surface rainfall (Hayden & Liu, 2021; You et al., 2019). As a result, widespread spurious heavy precipitation is retrieved over areas where true surface rainfall is weak or absent (STH <10 km). This process is a key reason why the IMERG precipitation footprint in Figure 1 is substantially broader than that observed by PMR.

The negative bias shown in Figure 3c when precipitation is stratified by storm-top height corresponds to the convective core regime on the right side of Figure 4 In these deep convective systems, cloud-top and storm-top heights are nearly aligned (STH ≈ CTH > 12 km), and radar profiles typically exhibit strong vertically coherent echoes, indicating extreme rainfall intensity and very high ice-water content. Under such conditions, once precipitation intensity and ice-phase particle concentration exceed a critical threshold, the high-frequency scattering

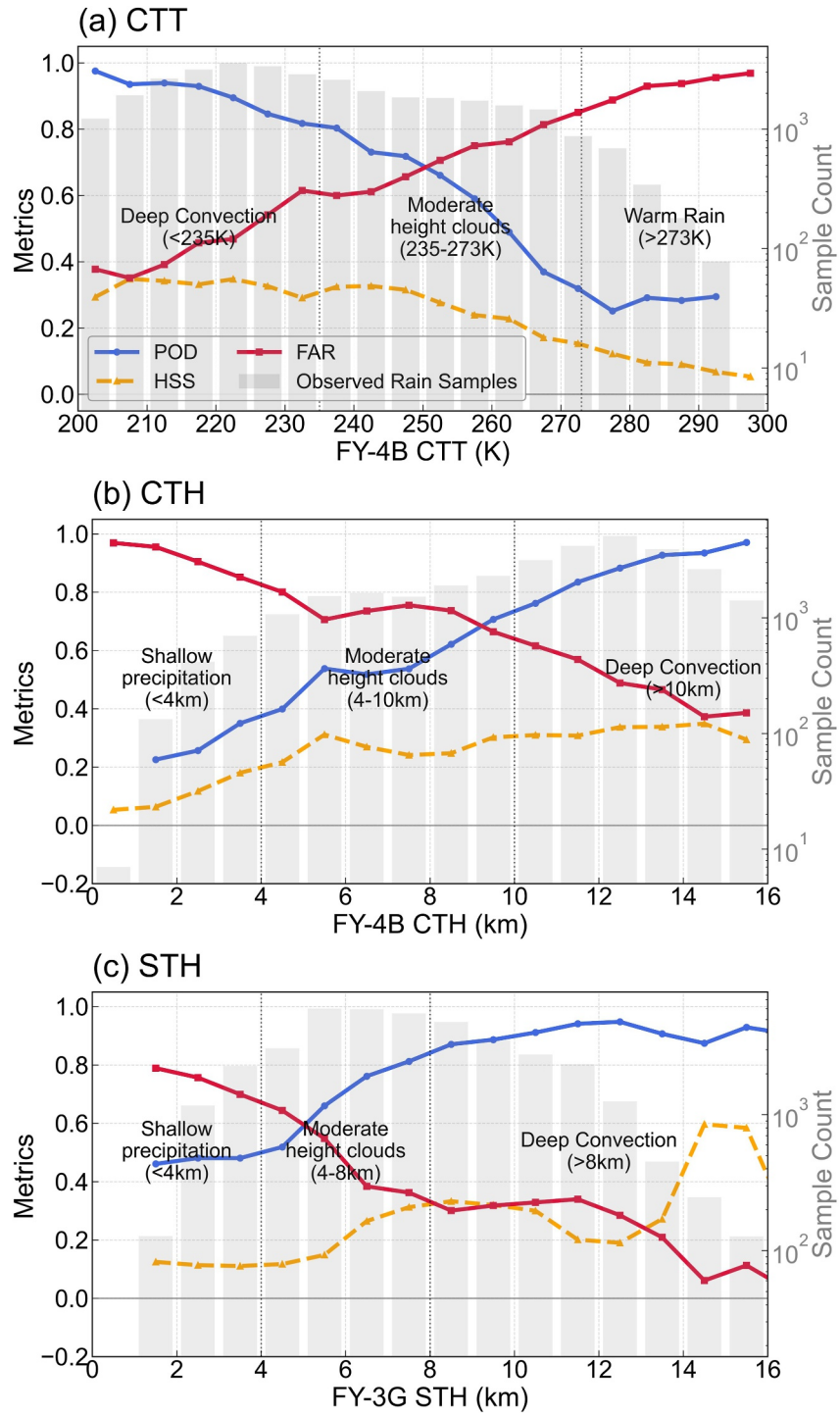


**Figure 2.** Variations in IMERG precipitation probability of detection (POD), Heidke Skill Score (HSS), and false alarm rate (FAR) with different classification variables. The gray bars, corresponding to the right logarithmic *y*-axis, represent the total number of observed rain samples within each bin, providing context for the statistical stability of the metric variations.

signal used by passive microwave retrievals becomes saturated. The associated brightness-temperature depression then no longer scales linearly with increasing rain rate (Petković et al., 2018), causing the retrieval algorithm to lose sensitivity to extreme precipitation. At the same time, the coarse fields of view of PMW sensors and the

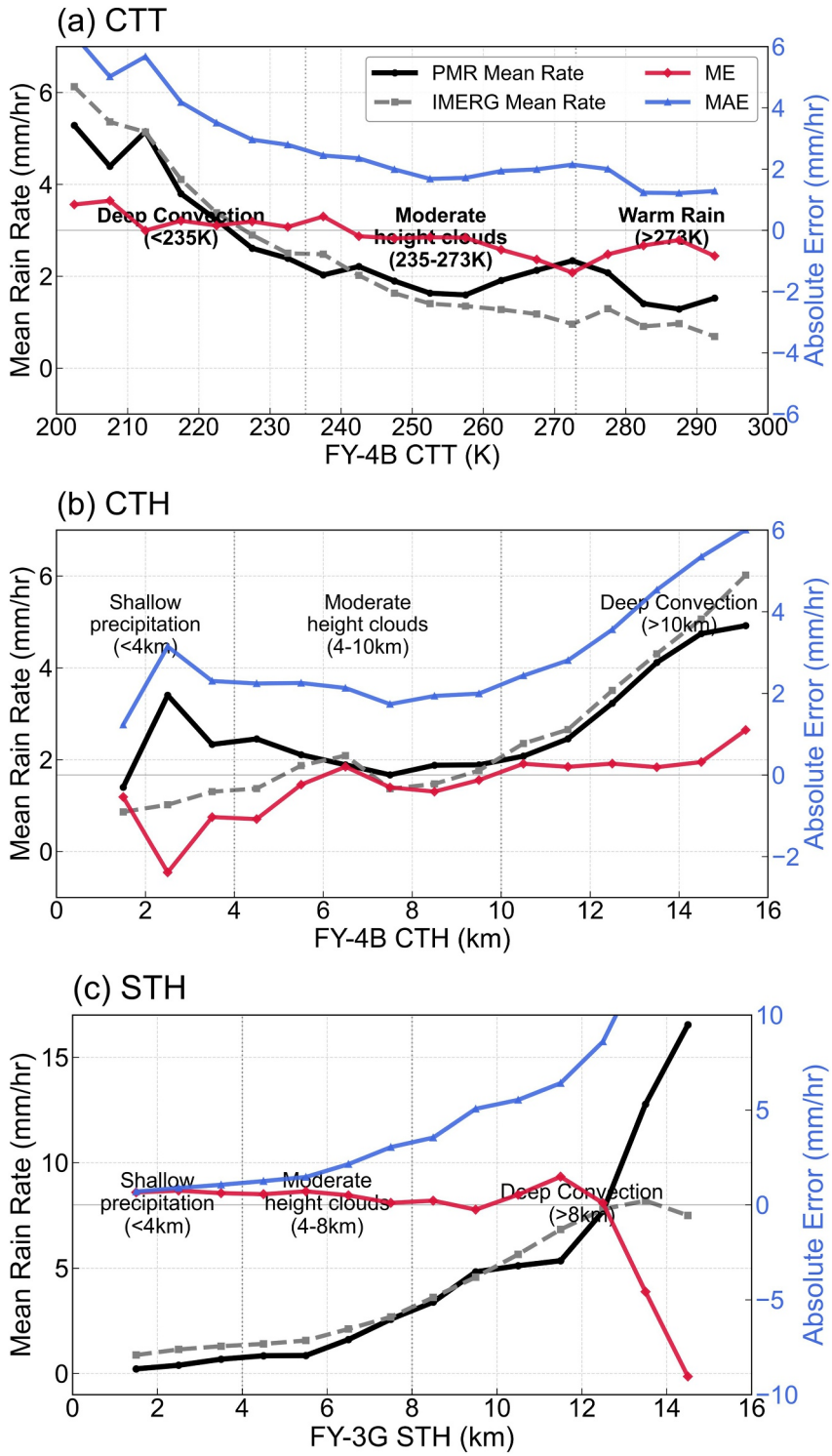


**Figure 3.** Variations in PMR and IMERG mean rain rates, together with the mean error (ME) and mean absolute error (MAE), as functions of different classification variables.

limited representation of extreme precipitation in the retrieval database may also contribute to the underestimation of intense convective rainfall. These factors lead directly to underestimation of precipitation intensity by IMERG in convective cores and explains the negative bias in the high-STH regime.

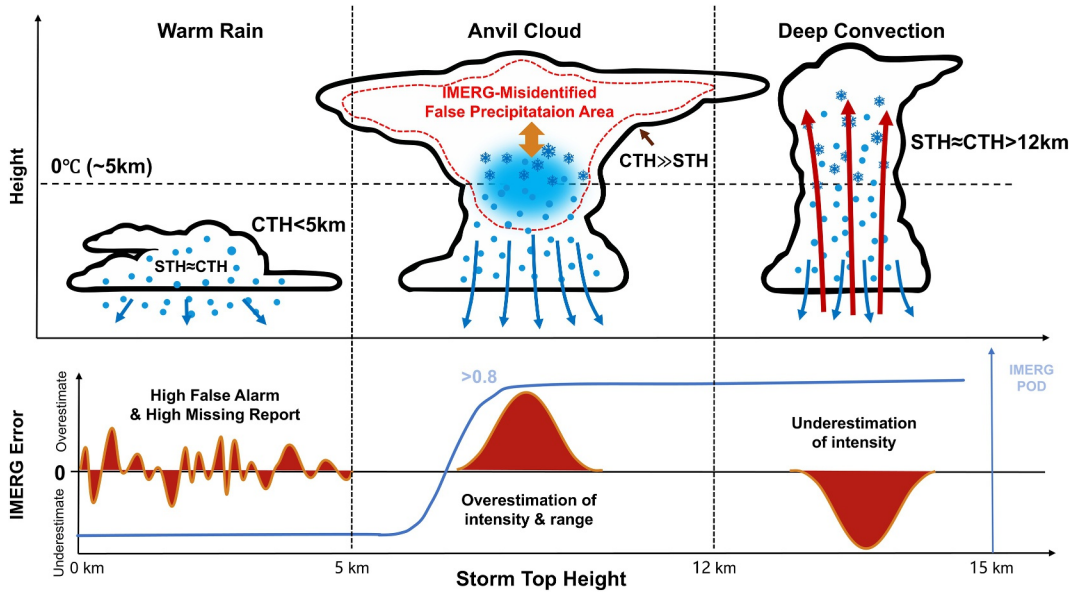


**Figure 4.** Conceptual schematic of IMERG precipitation estimation errors for different cloud–precipitation structures.

## 5. Conclusions

Using FY-3G PMR and FY-4B observations, this study investigates IMERG retrieval errors during the pre-summer rainy season in South China from the perspective of cloud-rain vertical structure. Three main conclusions are drawn:

1. IMERG intensity bias depends strongly on the chosen vertical reference.Deep precipitation systems are overestimated when classified by cloud-top parameters (CTH or CTT), but underestimated when classified by storm-top height. This sign reversal demonstrates that cloud-top information alone cannot adequately represent the true vertical structure of precipitation.
2. IMERG detection performance exhibits a clear vertical threshold.Probability of detection increases nonlinearly with STH and rises rapidly once STH exceeds 7.5 km, remaining above 0.8 thereafter. This indicates that the current algorithm detects precipitation reliably only after systems develop sufficient vertical extent above the freezing level, while shallow precipitation remains difficult to capture.
3. Three typical cloud-rain vertical-mismatch regimes explain the main IMERG retrieval errors: (a) missed warm-cloud precipitation (STH $\approx$ CTH $<$ 5 km), (b) overestimated precipitation area in anvil regions (CTH $\gg$ STH), and (c) underestimated precipitation intensity in convective cores (STH $\approx$ CTH $>$ 12 km). Together, these regimes show that cloud-rain height difference provides an effective physical framework for diagnosing and improving multisource satellite precipitation retrievals.

In summary, traditional correction methods based only on surface observations are insufficient to remove the systematic biases in satellite precipitation products. Recent studies suggest that combining storm-top information from active radar with cloud-top information from geostationary satellites provides a powerful physical constraint on the internal vertical structure of precipitation (Zhang et al., 2022). Moreover, accurate three-dimensional hydrometeor classification and vertical-structure profiling are essential for fine-scale characterization of heavy-precipitation systems (H. Chen et al., 2025). These results suggest that precipitation vertical structure, particularly the cloud–rain height difference, provides a useful physical diagnostic framework for understanding retrieval errors and may offer guidance for the future development of more physically informed multisource satellite precipitation algorithms. Such an approach could reduce spurious precipitation in anvil regions while alleviating intensity underestimation in deep convective cores. Future studies will feature independent evaluations of the PMW and IR components, with the ultimate goal of further untangling the specific physical attributions of IMERG retrieval biases. More broadly, this study highlights the value of active precipitation radars such as FY-3G for global water-cycle observation and provides an observational foundation for the design of next-generation synergistic precipitation retrieval algorithms.

## Conflict of Interest

The authors declare no conflicts of interest relevant to this study.

## Availability Statement

The data sets analyzed in this study are publicly available. The GPM IMERG V07 Final Run precipitation products are available from the NASA Goddard Earth Sciences Data and Information Services Center (Huffman et al., 2023). The FY-3G PMR data and FY-4B AGRI products are publicly available from the National Satellite Meteorological Centre (NSMC) of CMA (https://data.nsmc.org.cn/DataPortal/cn/data/overview.html). Cloud-top temperature (CTT) and cloud-top height (CTH) were obtained from the FY-4B atmospheric products, while the PMR precipitation and storm-top height (STH) data were derived from the Ku-band precipitation rate (KuR) product of the FY-3G atmospheric products.

**Acknowledgments**
This study was jointly supported by the Fengyun Application Pioneering Project (FY-APP-2024.0502), the National Natural Science Foundation of China (Grant 42105068 and 42475085), and an Innovation Group Project of the Southern Marine Science and Engineering Guangdong Laboratory (Zhuhai) (Grant 311022006).

## References

Chen, G., Lan, R., Zeng, W., Pan, H., & Li, W. (2018). Diurnal variations of rainfall in surface and satellite observations at the Monsoon Coast (South China). *Journal of Climate*, *31*(5), 1703–1724. https://doi.org/10.1175/JCLI-D-17-0373.1

Chen, H., Sun, T., Zhao, K., Chen, Y., Zhou, A., & Tong, C.-C. (2025). Dual-polarization radar data assimilation based on hydrometeor classification and its impact on severe weather prediction. *Journal of Geophysical Research: Atmospheres*, *130*(12), e2024JD042797. https://doi.org/10.1029/2024JD042797

Chen, S., Chen, T., & Cao, Y. (2025). Performance assessment of hourly precipitation products from IMERG and GSMaP over mainland China. *Torrential Rain and Disasters*, *44*, 1–14. https://doi.org/10.12406/byzh.2025-050

Cui, W., Dong, X., Xi, B., Feng, Z., & Fan, J. (2020). Can the GPM IMERG final product accurately represent MCSs' precipitation characteristics over the central and Eastern United States? *Journal of Hydrometeorology*, *21*(1), 39–57. https://doi.org/10.1175/JHM-D-19-0123.1

Derin, Y., Kirstetter, P.-E., Gourley, J. J., Derin, Y., Kirstetter, P.-E., & Gourley, J. J. (2021). Evaluation of IMERG satellite precipitation over the land–coast–ocean continuum. Part I: Detection. *Journal of Hydrometeorology*, *22*(11). https://doi.org/10.1175/JHM-D-21-0058.1

Dezfuli, A. K., Ichoku, C. M., Huffman, G. J., Mohr, K. I., Selker, J. S., van de Giesen, N., et al. (2017). Validation of IMERG precipitation in Africa. *Journal of Hydrometeorology*, *18*(10), 2817–2825. https://doi.org/10.1175/jhm-d-17-0139.1

Ferraro, R. R. (1997). Special sensor microwave imager derived global rainfall estimates for climatological applications. *Journal of Geophysical Research*, *102*(14), 16715–16735. https://doi.org/10.1029/97jd01210

Gong, J., & Wu, D. L. (2017). Microphysical properties of frozen particles inferred from global precipitation measurement (GPM) microwave imager (GMI) polarimetric measurements. *Atmospheric Chemistry and Physics*, *17*(4), 2741–2757. https://doi.org/10.5194/acp-17-2741-2017

Grecu, M., Olson, W. S., Munchak, S. J., Ringerud, S., Liao, L., Haddad, Z., et al. (2016). The GPM combined algorithm. *Journal of Atmospheric and Oceanic Technology*, *33*(10), 2225–2245. https://doi.org/10.1175/JTECH-D-16-0019.1

Guo, H., Tian, Y., Li, J., Guo, C., Meng, X., Wang, W., & De Maeyer, P. (2024). Has IMERG_V07 improved the precision of precipitation retrieval in mainland China compared to IMERG_V06? *Remote Sensing*, *16*(14), 2671. https://doi.org/10.3390/rs16142671

Guo, Z.-h., Chen, Y., Xiao, T.-g., & Zeng, Z.-l. (2024). Mesoscale and microphysical characteristics of a double rain belt event in south China on May 10–13, 2022. *Journal of Tropical Meteorology*, *30*(1), 61–75. https://doi.org/10.3724/j.1006-8775.2024.007

Han, B., Du, Y., Wu, C., & Liu, X. (2021). Microphysical characteristics of the coexisting frontal and warm-sector heavy rainfall in south China. *Journal of Geophysical Research: Atmospheres*, *126*(21), e2021JD035446. https://doi.org/10.1029/2021JD035446

Hayden, L., & Liu, C. (2021). Differences in the diurnal variation of precipitation estimated by spaceborne radar, passive microwave radiometer, and IMERG. *Journal of Geophysical Research: Atmospheres*, *126*(9), e2020JD033020. https://doi.org/10.1029/2020JD033020

He, R., Li, H., Luo, J., Huang, H., & Zhu, Y. (2025). Comparison of the reflectivities from precipitation measurement radar onboard the FY-3G satellite and ground-based S-Band dual-polarization radars. *Remote Sensing*, *17*(7), 1117. https://doi.org/10.3390/rs17071117

Hou, A. Y., Kakar, R. K., Neeck, S., Azarbarzin, A. A., Kummerow, C. D., Kojima, M., et al. (2014). The global precipitation measurement mission. *Bulletin of the American Meteorological Society*, *95*(5), 701–722. https://doi.org/10.1175/BAMS-D-13-00164.1

Huffman, G. J., Bolvin, D. T., Braithwaite, D., Hsu, K.-L., Joyce, R. J., Kidd, C., et al. (2020). Integrated multi-satellite retrievals for the global precipitation mea. *Advances in Global Change Research*, 343–353. https://doi.org/10.1007/978-3-030-24568-9_19

Huffman, G. J., Stocker, E. F., Bolvin, D. T., Nelkin, E. J., & Jackson, T. (2023). GPM IMERG final precipitation L3 half hourly 0.1 degree x 0.1 degree V07 [Dataset]. *Goddard Earth Sciences Data and Information Services Center (GES DISC)*. https://doi.org/10.5067/GPM/IMERG/3B-HH/07

Huo, J., Lu, D., Duan, S., Bi, Y., & Liu, B. (2020). Comparison of the cloud top heights retrieved from MODIS and AHI satellite data with ground-based Ka-band radar. *Atmospheric Measurement Techniques*, *13*(1), 1–11. https://doi.org/10.5194/amt-13-1-2020

Kidd, C., Kniveton, D. R., Todd, M. C., & Bellerby, T. J. (2003). Satellite rainfall estimation using combined passive microwave and infrared algorithms. *Journal of Hydrometeorology*, *4*(6). https://doi.org/10.1175/1525-7541(2003)004

Li, X., & Du, Y. (2021). Statistical relationships between two types of heavy rainfall and low-level jets in south China. *Journal of Climate*, *34*(21), 8549–8566. https://doi.org/10.1175/JCLI-D-21-0121.1

Liu, B., Li, H., Liu, L., Shang, J., Kuo, K.-S., Lu, C., et al. (2025). On the detection sensitivities of dual-frequency radars onboard FY-3G and GPM-CO. *Atmospheric Research*, *316*, 107935. https://doi.org/10.1016/j.atmosres.2025.107935

Liu, C., Zipser, E. J., & Nesbitt, S. W. (2007). Global distribution of tropical deep convection: Different perspectives from TRMM infrared and radar data. *Journal of Climate*, *20*(3), 489–503. https://doi.org/10.1175/JCLI4023.1

Liu, C.-Y., Chiu, C.-H., Lin, P.-H., & Min, M. (2020). Comparison of cloud-top property retrievals from advanced Himawari Imager, MODIS, CloudSat/CPR, CALIPSO/CALIOP, and radiosonde. *Journal of Geophysical Research: Atmospheres*, *125*(15), e2020JD032683. https://doi.org/10.1029/2020JD032683

Luo, Y., Zhang, R., Wan, Q., Wang, B., Wong, W. K., Hu, Z., et al. (2017). The Southern China monsoon rainfall experiment (SCMREX). *Bulletin of the American Meteorological Society*, *98*(5), 999–1013. https://doi.org/10.1175/BAMS-D-15-00235.1

Maranan, M., Fink, A. H., Knippertz, P., Amekudzi, L. K., Atiah, W. A., & Stengel, M. (2020). A process-based validation of GPM IMERG and its sources using a mesoscale rain gauge network in the West African Forest Zone. *Journal of Hydrometeorology*, *21*(4), 729–749. https://doi.org/10.1175/JHM-D-19-0257.1

Montoya Duque, E., Huang, Y., May, P. T., & Siems, S. T. (2023). An evaluation of IMERG and ERA5 quantitative precipitation estimates over the Southern Ocean using shipborne observations. *Journal of Applied Meteorology and Climatology*, *62*(11), 1479–1495. https://doi.org/10.1175/jamc-d-23-0039.1

Orenstein, J. A. (1982). Multidimensional tries used for associative searching. *Information Processing Letters*, *14*(4), 150–157. https://doi.org/10.1016/0020-0190(82)90027-8

Petersen, W. A., Kirstetter, P.-E., Wang, J., Wolff, D. B., & Tokay, A. (2020). The GPM ground validation program. In V. Levizzani, C. Kidd, D. B. Kirschbaum, C. D. Kummerow, K. Nakamura, & F. J. Turk (Eds.), *Satellite precipitation measurement: Volume 2* (pp. 471–502). Springer International Publishing. https://doi.org/10.1007/978-3-030-35798-6_2

Petković, V., Kummerow, C. D., Randel, D. L., Pierce, J. R., & Kodros, J. K. (2018). Improving the quality of heavy precipitation estimates from satellite passive microwave rainfall retrievals. *Journal of Hydrometeorology*, *19*(1), 69–85. https://doi.org/10.1175/JHM-D-17-0069.1

Pradhan, R. K., Markonis, Y., Pradhan, R. K., & Markonis, Y. (2023). Performance evaluation of GPM IMERG precipitation products over the tropical Oceans using buoys. *Journal of Hydrometeorology*, *24*(10). https://doi.org/10.1175/JHM-D-22-0216.1

Rajagopal, M., Zipser, E., Huffman, G., Russell, J., & Tan, J. (2021). Comparisons of IMERG version 06 precipitation at and between passive microwave overpasses in the tropics. *Journal of Hydrometeorology*, *22*(8). https://doi.org/10.1175/JHM-D-20-0226.1

Sekaranom, A. B., Masunaga, H., Sekaranom, A. B., & Masunaga, H. (2019). Origins of heavy precipitation biases in the TRMM PR and TMI products assessed with CloudSat and reanalysis data. *Journal of Applied Meteorology and Climatology*, *58*(1). https://doi.org/10.1175/JAMC-D-18-0011.1

Shang, J., Zhang, P., Cao, L., Wu, Q., Wang, X., Zhang, X., et al. (2025). Comparison of the precipitation measurement radar onboard the FY-3G meteorological satellite with ground-based radars in China. *Advances in Atmospheric Sciences*, *43*(3), 645–660. https://doi.org/10.1007/s00376-025-5149-3

Skofronick-Jackson, G., Petersen, W. A., Berg, W., Kidd, C., Stocker, E. F., Kirschbaum, D. B., et al. (2017). The global precipitation measurement (GPM) mission for science and society. *Bulletin of the American Meteorological Society*, *98*(8), 1679–1695. https://doi.org/10.1175/BAMS-D-15-00306.1

Smalley, M., L'Ecuyer, T., Lebsock, M., & Haynes, J. (2014). A comparison of precipitation occurrence from the NCEP stage IV QPE product and the CloudSat cloud profiling radar. *Journal of Hydrometeorology*, *15*(1). https://doi.org/10.1175/JHM-D-13-048.1

Stephens, G. L., Kummerow, C. D., Stephens, G. L., & Kummerow, C. D. (2007). The remote sensing of clouds and precipitation from space: A review. *Journal of the Atmospheric Sciences*, *64*(11). https://doi.org/10.1175/2006JAS2375.1

Tang, G., Clark, M. P., Papalexiou, S. M., Ma, Z., & Hong, Y. (2020). Have satellite precipitation products improved over last two decades? A comprehensive comparison of GPM IMERG with nine satellite and reanalysis datasets. *Remote Sensing of Environment*, *240*, 111697. https://doi.org/10.1016/j.rse.2020.111697

Tang, G., Ma, Y., Long, D., Zhong, L., & Hong, Y. (2016). Evaluation of GPM Day-1 IMERG and TMPA Version-7 legacy products over Mainland China at multiple spatiotemporal scales. *Journal of Hydrology*, *533*, 152–167. https://doi.org/10.1016/j.jhydrol.2015.12.008

Turk, F. J., Ringerud, S. E., Camplani, A., Casella, D., Chase, R. J., Ebtehaj, A., et al. (2021). Applications of a CloudSat-TRMM and CloudSat-GPM satellite coincidence dataset. *Remote Sensing*, *13*(12), 2264. https://doi.org/10.3390/rs13122264

Wang, D., Wang, X., Liu, L., Wang, D., Huang, H., & Pan, C. (2018). Evaluation of TMPA 3B42V7, GPM IMERG and CMPA precipitation estimates in Guangdong Province, China. *International Journal of Climatology*, *39*(2), 738–755. https://doi.org/10.1002/joc.5839

Wang, J., Petersen, W. A., & Wolff, D. B. (2021). Validation of satellite-based precipitation products from TRMM to GPM. *Remote Sensing*, *13*(9), 1745. https://doi.org/10.3390/rs13091745

Wernli, H., Paulat, M., Hagen, M., & Frei, C. (2008). SAL—A novel quality measure for the verification of quantitative precipitation forecasts. *Monthly Weather Review*, *136*(11), 4470–4487. https://doi.org/10.1175/2008MWR2415.1

Yang, X., Ge, J., Hu, X., Wang, M., & Han, Z. (2021). Cloud-top height comparison from multi-satellite sensors and ground-based cloud radar over SACOL site. *Remote Sensing*, *13*(14), 2715. https://doi.org/10.3390/rs13142715

You, Y., Meng, H., Dong, J., & Rudlosky, S. (2019). Time-lag correlation between passive microwave measurements and surface precipitation and its impact on precipitation retrieval evaluation. *Geophysical Research Letters*, *46*(14), 8415–8423. https://doi.org/10.1029/2019GL083426

Zhang, A., Chen, Y., Pan, X., Hu, Y., Chen, S., & Li, W. (2022). Precipitation microphysics of tropical cyclones over Northeast China in 2020. *Remote Sensing*, *14*(9), 2188. https://doi.org/10.3390/rs14092188

Zhang, P., Gu, S., Chen, L., Shang, J., Lin, M., Zhu, A., et al. (2023). FY-3G satellite instruments and precipitation products: First report of China's Fengyun rainfall Mission In-Orbit. *Journal of Remote Sensing*, *3*, 0097. https://doi.org/10.34133/remotesensing.0097

Zhang, Y., Zheng, X., Li, X., Lyu, J., & Zhao, L. (2023). Evaluation of the GPM-IMERG V06 final run products for monthly/annual precipitation under the complex climatic and topographic conditions of China. *Journal of Applied Meteorology and Climatology*, *62*(8), 929–946. https://doi.org/10.1175/JAMC-D-22-0110.1

Zuo, H., Chen, Y., Liu, T., Zhang, A., Chen, S., & Li, W. (2025). Frontal structure effects on precipitation microphysics in south China rain cells. *Journal of Geophysical Research: Atmospheres*, *130*(20), e2024JD043270. https://doi.org/10.1029/2024JD043270